

Cite this: *Nanoscale*, 2018, **10**, 19927

Highly sensitive detection of exosomes by 3D plasmonic photonic crystal biosensor[†]

Shuyan Zhu,^{a,b} Hualin Li,^{b,c} Mengsu Yang^{b,c} and Stella W. Pang^{ID, *a,b}

In this study, two-dimensional (2D), quasi-three-dimensional (3D), and 3D plasmonic photonic crystal (PPC) nanostructures with point-defect cavities were developed and fabricated using direct and reversal nanoimprint lithography. As a result of the hybrid coupling of localized surface plasmon resonance and Fabry–Perot cavity modes, the quasi-3D plasmonic nanoholes showed higher electromagnetic field intensity and sensitivity than the 2D plasmonic nanoholes. Specifically, the sensitivity of the quasi-3D plasmonic nanoholes was 483 nm per refractive index unit (RIU), whereas that of the 2D plasmonic nanoholes was 276 nm RIU⁻¹. In addition, by enhancing electromagnetic field intensity around corners and generating an additional subradiant dark mode, the symmetrical breakage of the quasi-3D plasmonic nanoholes further increased the sensitivity to 946 nm RIU⁻¹. Among all the nanostructures developed in the study, the 3D PPC nanostructures with point-defect cavities showed the highest sensitivity up to 1376 nm RIU⁻¹ and highest figure of merit of 11.6 as the result of the hybrid coupling of plasmonics and photonic crystal modes with multilayered plasmonic nanostructures. The spacing between the 3D PPC nanostructures was comparable with the average size of exosomes derived from fibroblast L cells, which allowed the exosomes to spread around the 3D PPC nanostructures with increased sensing area. This effect further enhanced the detection sensitivity with a large peak shift of 9 nm when using the 3D PPC biosensor to detect exosomes at the concentration of 1×10^4 particles per ml, and the peak shift increased to 102 nm as exosome concentration increased to 1×10^{11} particles per ml.

Received 30th August 2018,
Accepted 16th October 2018

DOI: 10.1039/c8nr07051b

rsc.li/nanoscale

1. Introduction

Exosomes are small cell-derived vesicles that are typically 30–300 nm in size.¹ They carry the same mRNA, DNA, and signal lipids as their origin cells and have important roles in cell-to-cell communication.² Cancer cells release more exosomes than normal cells, and specific exosome biomarkers like TGFβ1 and glyican-1 could enhance endothelial cell migration and promote cell metastases and proliferation.^{3,4} In contrast to circulating tumor cells (CTCs), which are rarely observed and are present in patients with cancer at concentrations of less than 10 CTCs per ml concentration, exosomes are more accessible. Thus, they are promising targets of non-invasive methods for cancer detection and diagnosis.^{5–7} Despite their potential clinical applications, their small sizes complicate

their quantitative detection. Various detection methods, such as flow cytometry, electrochemical and mechanical transduction, and nanoparticle tracking analysis (NTA), have been employed for exosome detection. Nevertheless, these methods all have some limitations. Flow cytometry cannot detect nanoparticles (NPs) that are less than 300 nm in diameter without fluorescence labeling.⁸ Electrochemical biosensors encounter the problem of high background noise and require large sample volumes for detection.⁹ Atomic force microscopy can be used to detect NPs at high resolution. However, the scanning process of this method is time consuming.¹⁰ NTA is the most popular exosome detection method, but its detection range is limited to 2×10^8 – 2×10^9 particles per ml.¹¹ By contrast, localized surface plasmon resonance (LSPR)-based optical biosensors are highly sensitive to the change in local refractive index (RI) around a plasmonic sensor area, and its decay length is as low as 100 nm.^{12,13} These characteristics make LSPR a suitable approach for exosome detection. Moreover, it is rapid, highly sensitive, and has high signal-to-noise ratio.¹⁴ Therefore, we proposed a novel highly sensitive LSPR biosensor for quantitative exosome detection.

LSPR occurs when the collective oscillation of free electrons in noble metal NPs is resonant with the incident light frequency. This effect results in the strong confinement of

^aDepartment of Electronic Engineering, City University of Hong Kong, Hong Kong, China. E-mail: pang@cityu.edu.hk

^bCentre for Biosystems, Neuroscience, and Nanotechnology, City University of Hong Kong, Hong Kong, China

^cDepartment of Biomedical Sciences, City University of Hong Kong, Hong Kong, China

[†]Electronic supplementary information (ESI) available. See DOI: 10.1039/c8nr07051b

surface plasmons (SPs) on the surface of NPs. Intensely localized SPs are highly sensitive to the changes in effective RI in the surrounding area and could be used to detect exosomes at low concentration with high sensitivity. Recently, a three-dimensional (3D) plasmonic nanobowl was utilized to detect 20 μl of exosomes at the concentration of 580 fM through surface-enhanced Raman spectroscopy.¹⁵ A nanoplasmonic exosome biosensor based on two-dimensional (2D) gold (Au) nanoholes with diameter of 200 nm and pitch of 450 nm demonstrated a detection limit up to 670 aM.¹⁶ The performance of LSPR biosensors is determined by their refractive index sensitivity (RIS) and figure of merit (FOM).

To increase the RIS and FOM of plasmonic biosensors, most researchers have focused on changing the shapes of plasmonic nanostructures because LSPR spectra are highly dependent on nanostructure size, geometry, distribution, and effective RI in the surrounding area. 2D plasmonic nanostructures, such as Au nanodots^{17,18} and nanoholes,¹⁹ had been investigated widely. Nevertheless, their plasmon modes, which are only coupled with adjacent nanostructures in the 2D area, limit their sensitivity and FOM to 450 nm per refractive index unit (RIU) and 1.8, respectively. Furthermore, the modes of Au nanodots and nanoholes are superradiant plasmon modes excited by normal incident light. Thus, their localized SPs would attenuate exponentially, and the radiant damping effect of this superradiant plasmon mode would result in a large full width at half maximum (FWHM), which lowers the FOM for the resonance peak spectra.²⁰ Quasi-3D plasmonic nanostructures that consist of two different plasmonic layers could increase the intensity of localized SPs and RIS through the hybrid coupling of LSPR and Fabry-Perot cavity modes. For example, the sensitivity of quasi-3D nanoholes with Au nanoholes on top and Au nanodots at the bottom (483 nm RIU⁻¹) is higher than that of 2D Au nanoholes (276 nm RIU⁻¹). Quasi-3D nanostructures with Au nanosquares on top and Au nanoholes at the bottom achieve the high sensitivity of 496 nm RIU⁻¹.²¹ In contrast to Au nanodots and nanoholes, asymmetrical 2D nanostructures, such as nanorods,²² nanostars,²³ split-rings,²⁴ and ring/disk cavities,²⁵ could generate a subradiant dark mode, which is excited by the superradiant bright mode. This mode narrows the spectral line width and increases sensitivity to 780 nm RIU⁻¹ due to inhibition of radiant losses.

Given that asymmetrical nanostructures show higher electromagnetic (EM) field intensity and sensitivity than symmetrical nanostructures,^{26–28} asymmetrical quasi-3D and 3D nanostructures have also been investigated. Vertical split-ring nanostructures could lift localized SPs off the substrate and have the high sensitivity of 603 nm RIU⁻¹.²⁹ A nano Lycurgus cup array containing metal NPs on the sidewall of quasi-3D nanoholes exhibit the bifunctional capabilities of colorimetric and plasmonic sensing with the sensitivity of 796 nm RIU⁻¹.³⁰ Asymmetrical quasi-3D nanoholes could enhance EM field intensity around the sharp corners of the asymmetrical nanostructures and provide the sensitivity of 946 nm RIU⁻¹. A 3D disk in volcano arrays presented the high sensitivity of 977 nm

RIU⁻¹, which is attributed to the strong plasmonic coupling in the small gaps between the disk and volcano.³¹ The sensitivity of 3D chiral-shaped NPs could increase to 1091 nm RIU⁻¹ by engineering the dispersion function of plasmonic materials.³² To further increase the sensitivity of plasmonic biosensors, we have developed novel 3D plasmonic photonic crystal (PPC) nanostructures with point-defect cavities to confine and enhance EM field intensity through the hybrid coupling of plasmonic and photonic crystal modes. The sensitivity of these novel nanostructures increased to 1376 nm RIU⁻¹ for the resonance peak at 1232 nm. Moreover, these nanostructures exhibited the high FOM of 11.6 for the resonance peak at 564 nm. The 3D PPC biosensor was used to detect 10 μl of fibroblast L cell-derived exosomes with concentrations of 1×10^4 – 1×10^{11} particles per ml and exhibited a large peak shift of 9 nm during the detection of 1×10^4 particles per ml exosomes. To the best of our knowledge, this is the first investigation of 3D PPC nanostructures with point-defect cavities fabricated through reversal nanoimprint lithography and their application in quantitative exosome detection.

2. Experiment and methods

2.1 Fabrication of 2D, quasi-3D, and 3D PPC nanostructures

The 2D plasmonic nanoholes were fabricated through nanoimprint lithography and lift-off. As shown in ESI Fig. S1,† glass was first coated with poly(methyl methacrylate) (PMMA) and TU-7 polymer. The TU-7 polymer was imprinted using a silane-treated intermediate polymer stamp (IPS) soft stamp with nanosquare holes and the width, pitch, and depth of 280, 535, and 500 nm, respectively. The imprinting was carried out at 75 °C, 3 kTorr, and ultraviolet (UV) exposure for 10 s. The fabrication details of the IPS soft stamp and glass pretreatment are described in our previous paper.²¹ After imprinting, the TU-7 residual layer and PMMA were etched using an O₂/SF₆-reactive ion etching (RIE) with 50/2 sccm flow rates, 20 mTorr pressure, and 100 W rf power to access the bottom layer. The etch rate for the PMMA was higher than that used for the TU-7 polymer to create an undercut profile for the lift-off process, as shown in ESI Fig. S2.† After 2 nm chromium (Cr) and 20 nm Au films were evaporated at a tilt angle of 10°, lift-off was performed by immersing the samples for 1 min in resist remover PG (MicroChem Corp., USA) at 60 °C to generate the 2D asymmetrical Au nanoholes.

Quasi-3D plasmonic nanoholes were also fabricated using the same IPS soft stamp. TU-7 nanosquares with the width, pitch, and depth of 280, 535, and 500 nm, respectively, were first imprinted on a PMMA-coated Si substrate, then dry etched to the bottom layer. Symmetrical and asymmetrical Cr nanoholes were formed on Si through the normal and 10° tilt angle evaporation of 20 nm Cr and lift-off, respectively. Subsequently, symmetrical and asymmetrical Cr nanoholes were used as masks to etch the Si substrate with a deep RIE system (SPTS Technologies Ltd, USA) with 70/35 sccm C₄F₈/SF₆, 10 mTorr pressure, 10 W platen power, and 600 W coil

power. Symmetrical and asymmetrical quasi-3D Si nanohole stamps were replicated onto the IPS soft stamps. The use of the soft stamp could enable contamination control and prevent damage to the master Si stamp. Symmetrical quasi-3D nanoholes were 350 nm in diameter, 535 nm in pitch, and 350 nm in depth. Asymmetrical quasi-3D nanoholes had radii of 350 nm, pitch of 535 nm, and depth of 350 nm. Finally, 2 nm Cr and 20 nm Au films were thermally evaporated on these quasi-3D nanostructures to form two different plasmonic layers.

The 3D PPC nanostructures with point-defect cavities were fabricated by stacking SU-8 nanosquares on top of quasi-3D SU-8 nanoholes through reversal nanoimprint lithography. SU-8 polymer was used instead of TU-7 because SU-8 showed better adhesion than TU-7 after crosslinking. The top nanosquares and bottom quasi-3D nanoholes had the same hexagonal arrangement and pitch. The fabrication details of the stacked SU-8 nanostructures are described in our previous paper.^{33–37} Photonic crystal with point-defect cavities could be generated by stacking SU-8 nanosquares on top of the quasi-3D nanoholes because the diameters of the nanosquares are smaller than those of nanoholes. The nanosquares directly on top of the nanoholes were removed because they lacked contact surfaces. Finally, 2 nm Cr and 20 nm Au films were thermally evaporated in normal incidence to these 3D nanostructures at a vacuum of 1×10^{-6} Torr to generate the 3D PPC biosensor with three different plasmonic layers. No metallic films were deposited on the side-walls of the 3D nanostructures because the metal films were evaporated at low pressure with long mean free path and total film thickness was small.³⁸ A scanning electron microscope (SEM) (Hitachi SU5000, Japan) was used to acquire micrographs of 2D, quasi-3D, and 3D PPC nanostructures with point-defect cavities.

2.2 Measurement of RIS

A UV-visible-near infrared spectrophotometer (PE Lambda 750, PerkinElmer, USA) was used for the optical measurements. The samples were illuminated by a normal incident light source with wavelengths of 400–2400 nm, and the transmission spectra were collected with a photomultiplier. The RIS was measured by immersing the samples in certified RI liquids (Cargille Laboratories, USA) with RI values of 1.30, 1.33, 1.36, and 1.39.

2.3 Exosome isolation and quantification

Activated conditioned medium was collected from fibroblast L cells that had been starved for 48 h. To isolate cell debris, the medium was first centrifuged at 1000g (Kubota 2420, Japan) for 10 min and then at 100 000g (Beckman optima xe-90, USA) twice for 180 min. Afterwards, the exosome solution was diluted with phosphate-buffered saline (PBS) and spun at 100 000g for 70 min to isolate exosomes from soluble proteins. Exosomes with different concentrations were quantified with NTA system (LM10, Nanosight) and refrigerated at 4 °C.

2.4 Surface modification and exosome detection

The 3D PPC biosensor was treated with an O₂ plasma to make them hydrophilic and then treated with 20 µl of 10 µg ml⁻¹ of streptavidin (SA) at room temperature for 2 h. The SA was immobilized on the surface of the 3D PPC biosensor *via* thiol-Au reaction. After the removal of excess SA with PBS, the biosensor was mixed with 20 µl of biotinylated anti-epithelial cell adhesion molecule (anti-EpCAM) (10 µg ml⁻¹ in PBS with 1% (w/v) bovine serum albumin and 0.09% (w/v) sodium azide) and incubated for 1 h. After washing with PBS, the biosensor was loaded with 10 µl of exosome solution with different concentrations and incubated for 3 h. The captured exosomes were fixed with 0.05% glutaraldehyde and 2% paraformaldehyde in PBS for 1 h, washed with a graded series of methanol (70%, 80%, 90%, and 100%) and air-dried.

2.5 Numerical calculations through finite-difference time-domain method

Numerical finite-difference time-domain (FDTD) solutions (Lumerical Inc., Canada) were employed to simulate the EM field intensity distributions of 2D, quasi-3D, and 3D PPC nanostructures. The simulations were performed in the 3D area, and a plane wave with a wavelength of 400–2400 nm was used to illuminate the plasmonic nanostructures. The simulation region in the x-y plane was 9 µm², and periodic boundary conditions were set in the x- and y-directions. Perfectly matched layers (PML) were applied to minimize reflection errors in the top and the bottom boundaries along the z-direction. Frequency-domain profile monitors were placed near the plasmonic layers to collect the EM field profile in the resonance wavelength. The size and the distribution of the 2D, quasi-3D, and 3D PPC nanostructures were obtained from the SEM measurements, and a mesh size of 2 nm was used around the plasmonic layers. The dielectric constants for Au were obtained from a chemical handbook,³⁹ and the RI of SU-8 polymer was set as 1.61 in the simulations.⁴⁰ The mode profiles of the asymmetrical Au nanoholes were calculated using a finite difference eigenmode solver (Lumerical MODE solutions). The size of the asymmetrical Au nanoholes was the same as the ones used for the FDTD solutions, and the PML absorbing boundary conditions were set in the xyz directions.

3. Results and discussion

3.1 Simulation and experimental results of 2D and quasi-3D symmetrical and asymmetrical Au nanoholes

In the 2D Au nanoholes, surface plasmon polaritons (SPPs) and LSPR are supported, and SPs could propagate along the Au-dielectric interface and localize at the edges of the Au nanoholes.⁴¹ The simulated EM field intensity distribution for the symmetrical and asymmetrical 2D and quasi-3D Au nanoholes at resonance wavelength is depicted in Fig. 1. The diameter, pitch, and Cr/Au thickness of the symmetrical Au nanoholes were 350, 535, and 2/20 nm, respectively, as shown in Fig. 1(a and c). The asymmetrical Au nanoholes had the radii of

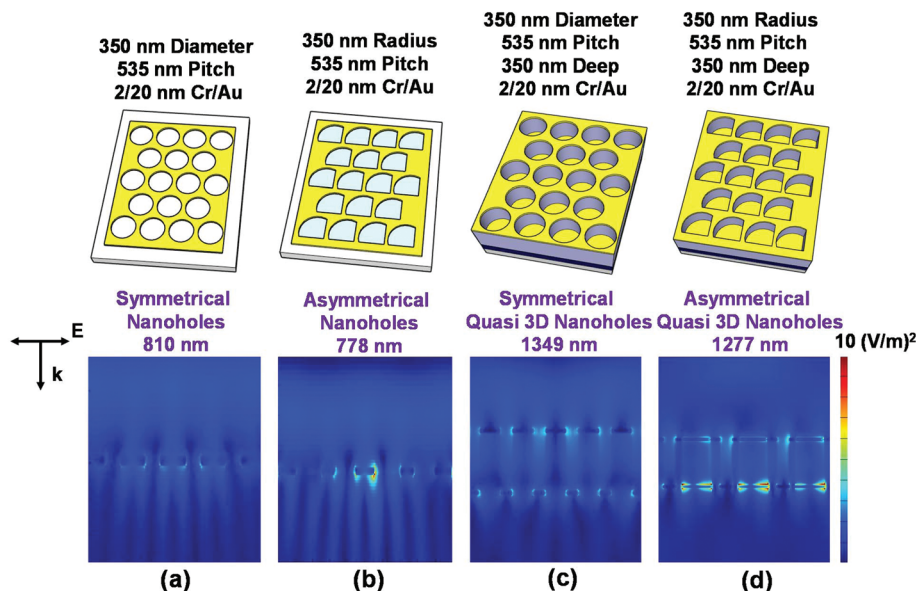


Fig. 1 Simulated electromagnetic field intensity distributions for (a) symmetrical Au nanoholes, (b) asymmetrical Au nanoholes, (c) symmetrical quasi-3D Au nanoholes, and (d) asymmetrical quasi-3D Au nanoholes.

350 nm, pitch of 535 nm, and Cr/Au thickness of 2/20 nm, as shown in Fig. 1(b and d). The depths of symmetrical and asymmetrical quasi-3D nanoholes were both 350 nm. As shown in Fig. 1, electronic charges around the sharp corners of asymmetrical Au nanoholes provided high EM field intensity. The strong localized EM field intensities in asymmetrical nanoholes are responsible for the higher sensitivity of asymmetrical nanostructures than that of symmetrical nanostructures. Furthermore, as shown in Fig. 1(c and d), quasi-3D Au nanoholes that consisted of Au nanoholes on top and Au nanodots at the bottom created Fabry–Perot cavities to further enhance EM field intensity through the hybrid coupling of LSPR and Fabry–Perot modes.⁴² This effect resulted in the higher EM field intensity and RIS of the quasi-3D nanoholes than that of the 2D Au nanoholes.

The micrograph, measured extinction spectra, RIS, and linear dependence of resonance wavelength on the RI of the surrounding area of the asymmetrical 2D Au nanoholes with the length, width, pitch, and Cr/Au thickness of 380, 280, 535, and 2/20 nm, respectively, are illustrated in Fig. 2(a1-a4). As shown in Fig. 2(a2), two resonance peaks at 661 and 814 nm were observed, and the resonance peak at 661 nm was attributed to the SPPs that could be derived from the following equation:⁴³

$$\lambda_{\text{SPPs}} = \frac{P}{\sqrt{\frac{3}{4}(i^2 + j^2 + j^2)}} \sqrt{\frac{\epsilon_d \epsilon_m}{\epsilon_d + \epsilon_m}} \quad (1)$$

where P is the periodicity of the 2D hexagonal lattice; i and j are integer numbers; and ϵ_d and ϵ_m are dielectric and metal constants, respectively. As shown by this equation, the SPPs are strongly dependent on periodicity instead of RI alteration in the surrounding area. In contrast to SPPs, the LSPR mode of

Au nanoholes was excited at the ridges of the holes and was highly sensitive to the changes in the geometry and distribution of Au nanoholes and to the changes in the RI in the surrounding area. As shown in Fig. 2(a3 and a4), the resonance peak at 814 nm linearly red-shifted as the RI increased from 1.30 to 1.39 and exhibited the sensitivity of 276 nm RIU^{-1} , which was attributed to the LSPR mode of Au nanoholes. ESI Fig. S1† shows the fabrication technology for the asymmetrical 2D Au nanoholes. TU-7 nanosquares were generated through nanoimprint lithography, and PMMA was etched in an O₂/SF₆ plasma, followed by the angle evaporation of 2/20 nm Cr/Au films on the substrate. After lifting off the TU-7 and PMMA layers, asymmetrical Au nanoholes were patterned on the glass substrate, as shown in Fig. 2(a1).

The micrograph, measured extinction spectra, RIS, and linear dependence of resonance wavelength on the RI of the surrounding area of the symmetrical quasi-3D Au nanoholes are shown in Fig. 2(b1-b4). Compared with that of the asymmetrical 2D Au nanoholes, the highest resonance peak of the symmetrical quasi-3D nanoholes was red-shifted to 1406 nm because of the hybrid plasmon coupling of the top Au nanoholes, bottom Au nanodots, and the Fabry–Perot cavity modes. The measured sensitivity of the 1406 nm resonance peak of the symmetrical quasi-3D Au nanoholes was 483 nm RIU^{-1} , which was higher than that of the asymmetrical 2D Au nanoholes (276 nm RIU^{-1}). This result indicates that introducing Au nanodots in LSPR and Fabry–Perot cavity modes could be used to tune the resonance wavelength from 814 nm to 1406 nm and increase sensitivity by enhancing EM field intensity. The resonance peaks as a function of RI in the surrounding medium are shown Fig. 2(b4), and the measured sensitivity of the 674 nm resonance peak was 100 nm RIU^{-1} . The symmetrical breakage of quasi-3D Au nanoholes could further

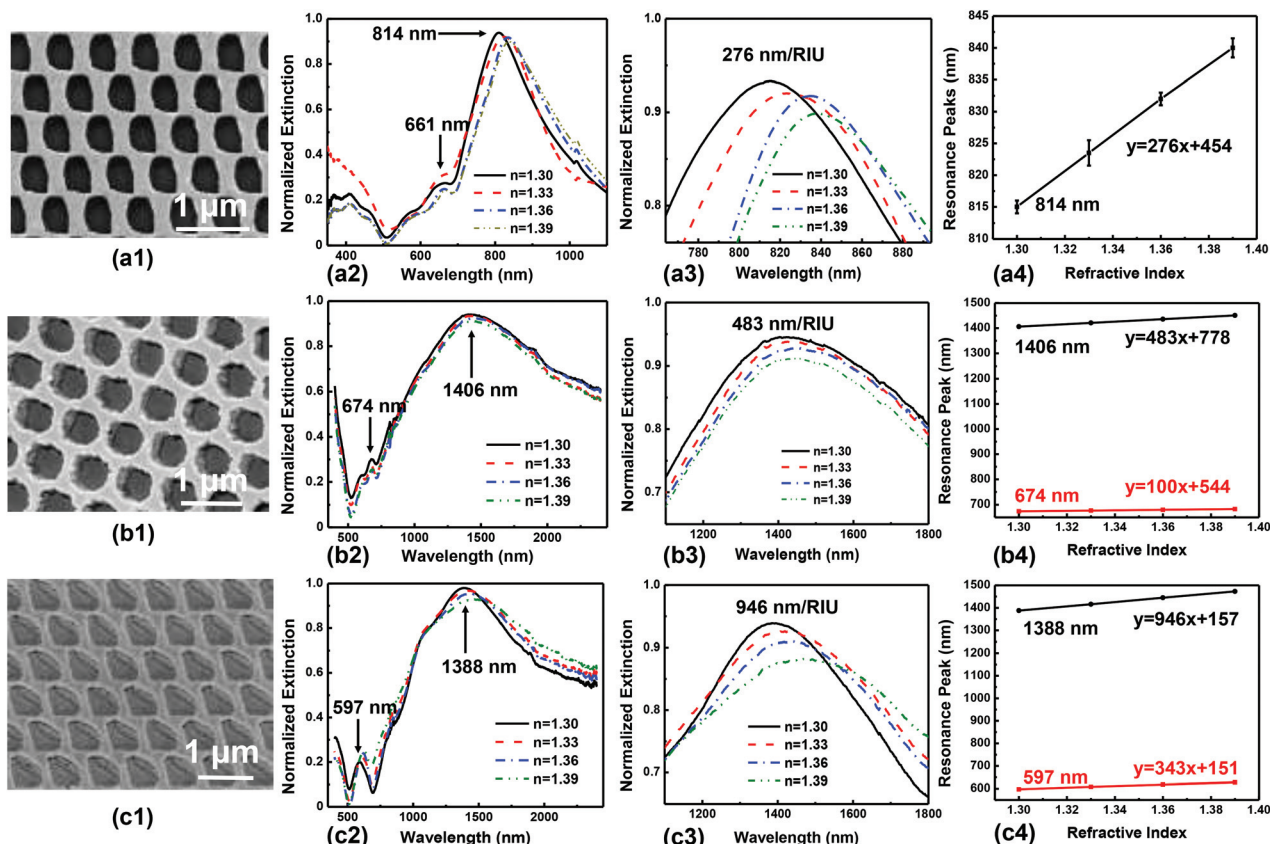


Fig. 2 Micrographs, normalized extinction, refractive index sensitivity, and resonance peak as function of refractive index (RI) of certified RI liquids for (a1–a4) asymmetrical 2D Au nanoholes with 380 nm length, 280 nm width, 535 nm pitch, and 2/20 nm Cr/Au thickness, (b1–b4) symmetrical quasi-3D Au nanoholes with 350 nm diameter, 535 nm pitch, 350 nm deep, and 2/20 nm Cr/Au thickness, and (c1–c4) asymmetrical quasi-3D Au nanoholes with 350 nm radius, 535 nm pitch, 350 nm deep, and 2/20 nm Cr/Au thickness.

enhance EM field intensity around corners and generate an additional quadrupole plasmon mode, which is a subradiant mode.^{20,44} As shown in ESI Fig. S3,† dipole resonance mode was excited for symmetrical quasi-3D Au nanoholes and the quadrupole plasmon mode was generated for asymmetrical quasi-3D Au nanoholes.^{45,46} Four hot spots were observed in the near-field intensity distribution of the asymmetrical quasi-3D Au nanoholes, indicating the presence of higher order quadrupole plasmon mode.^{27,47} In addition, the eigenmodes of the top asymmetrical Au nanoholes at resonance wavelength were simulated and both dipole and quadrupole modes were present, as shown in ESI Fig. S3(c).†

The micrograph, measured extinction spectra, RIS, and linear dependence of resonance wavelength on the RI of the surrounding area of the asymmetrical quasi-3D Au nanoholes are presented in Fig. 2(c1–c4). As shown in Fig. 2(c2 and c4), the asymmetrical quasi-3D Au nanoholes showed two resonance peaks at 597 and 1388 nm with the sensitivity of 343 and 946 nm RIU⁻¹, respectively; both of these values are higher than the sensitivity of symmetrical quasi-3D Au nanoholes. The EM field intensity and linewidth of symmetrical quasi-3D Au nanoholes were lower and broader than asymme-

trical quasi-3D Au nanoholes, because of their radiative damping losses and shorter plasmon lifetime caused by superradiant dipole mode.⁴⁸ Moreover, the coupling of subradiant and superradiant plasmon modes in the asymmetrical quasi-3D Au nanoholes could further narrow its spectral line shape and increase the FOM to 2.4, which is higher than the FOM of 0.8 exhibited by the symmetrical quasi-3D Au nanoholes, shown in Fig. 2(b3 and c3). The subradiant quadrupole plasmon mode of asymmetrical quasi-3D Au nanoholes was excited by the dipole resonance mode rather than the normal incident light which could effectively suppress radiative damping loss and result in higher EM field intensity and longer plasmon lifetime.^{45,49} All these results confirmed that the hybrid coupling of double-layer plasmonic nanostructures increased EM field intensity and sensitivity to levels higher than those exhibited by single-layer plasmonic nanostructures. In addition, the asymmetrical plasmonic nanostructures could further enhance the performance of the LSPR biosensor relative to that of symmetrical plasmonic nanostructures with identical hexagonal arrangement because of the higher EM field intensity and narrower spectra line width resulted by symmetrical breakage of plasmonic nanostructures.

3.2 3D PPC nanostructures

As shown in Fig. 1 and 2, the introduction of additional Au nanodots to the bottom of the quasi-3D Au nanoholes could create a Fabry–Perot cavity which couples with the LSPR modes to enhance EM field intensity and sensitivity. Following this idea, placing Au nanosquares on the top of the quasi-3D Au nanoholes could further enhance the EM field and sensitivity of three-layer plasmonic nanostructures relative to those of the quasi-3D nanostructures. Quasi-3D SU-8 nanosquares were reverse-imprinted on the surfaces of the quasi-3D nanoholes to support Au nanosquares on top and break the symmetrical quasi-3D Au nanoholes into asymmetrical nanostructures. The top quasi-3D SU-8 nanosquares could also be used as a photonic crystal nanostructure. The combination of plasmonic and photonic crystal nanostructures enabled strong spatial EM field confinement and efficiently enhanced light–matter interaction in the 3D PPC nanostructures.^{50,51} Fig. 3(a) shows the schematic of 3D PPC nanostructures and photonic crystal mode excited by the multiple plasmonic layers.^{51,52} To further enhance the EM field intensity of the 3D PPC nanostructures, we designed point-defect cavities to confine the EM field around the defect regions through the combination of distributed Bragg reflection and internal reflection,⁵³ as shown in Fig. 3(b). Light trapping in the 3D PPC nanostructures with point-defect cavities was caused by light scattering from the top Au nanosquares and SPPs between the Au nanoholes and dielectrics.⁵⁴ Three Au plasmonic layers with two SU-8 dielectrics in between could satisfy the condition for total internal

reflection because the RI of Au is lower than that of the SU-8 in the visible and near-infrared regions.⁵⁰

The fabrication technology of the 3D PPC nanostructures with point-defect cavities is shown in Fig. 4(a). The top SU-8 nanosquares had the width, pitch, and depth of 250, 535, and 450 nm, respectively. The bottom quasi-3D nanoholes had the width, pitch, and depth of 350, 535, and 350 nm, respectively. Reversal nanoimprint lithography was utilized to stack the top nanosquares on the surface of quasi-3D nanoholes with the identical hexagonal arrangement. After the removal of the residual layer, a moire pattern was formed, and point-defect cavities could be generated at areas where the top nanosquares were placed directly on top of the nanoholes because the top nanosquares were smaller than the bottom nanoholes which were removed due to lack of surface contact. The micrographs of the 3D PPC nanostructures with point-defect cavities are shown in Fig. 4(b).

The schematic of 3D PPC nanostructures and rotation angle between top nanosquares and bottom nanoholes is presented in Fig. 5(a). The top nanosquares and bottom nanoholes have a rotational periodicity of $\pi/3$ due to the hexagonal layout. The simulated EM field intensity distribution of the 3D PPC nanostructures with point-defect cavities and different rotation angles are illustrated in Fig. 5(b). For the resonance peak at longer wavelength, the EM field intensity was mainly enhanced around the point-defect cavities of the top and middle plasmonic layers. The results showed that the resonance peak wavelength changed slightly with rotation, but the EM field intensity of the three different plasmonic layers remained similar.

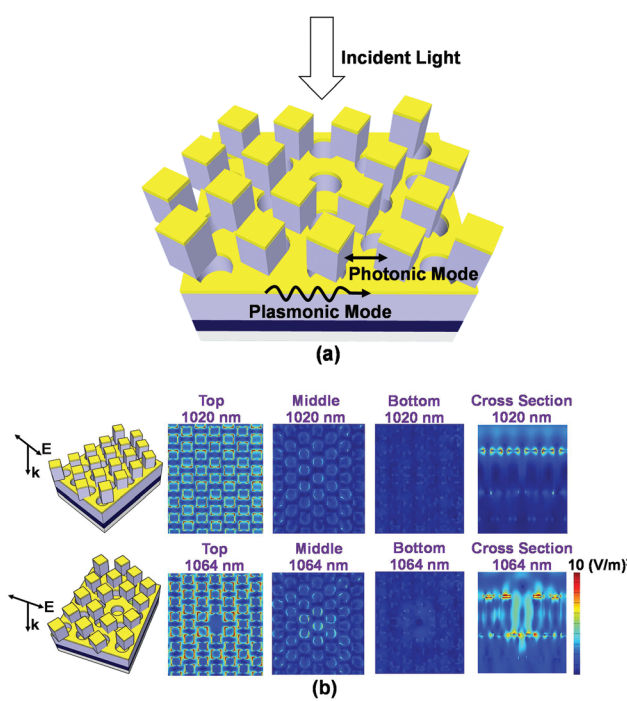


Fig. 3 (a) Schematic of 3D plasmonic photonic crystal nanostructures. (b) Simulated electromagnetic field intensity distributions of 3D plasmonic photonic crystal nanostructures without and with point-defect cavities.

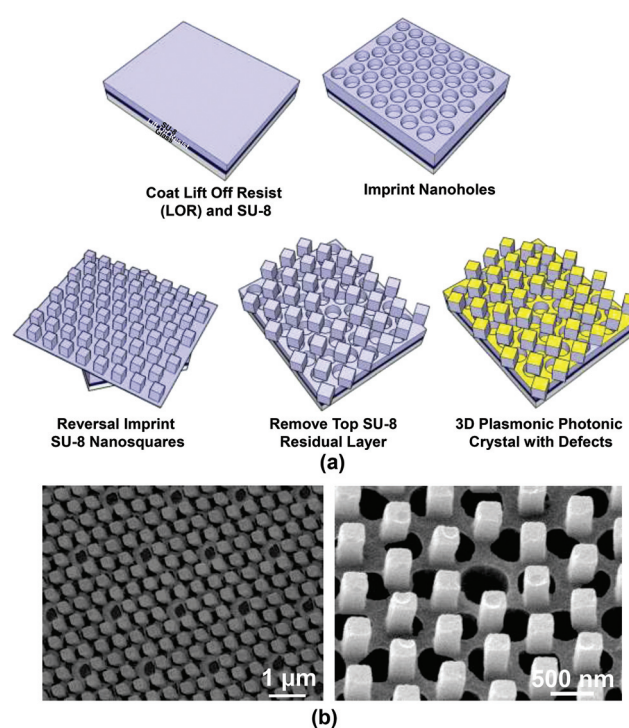


Fig. 4 (a) Fabrication technology and (b) micrographs of 3D plasmonic photonic crystal nanostructures with point-defect cavities.

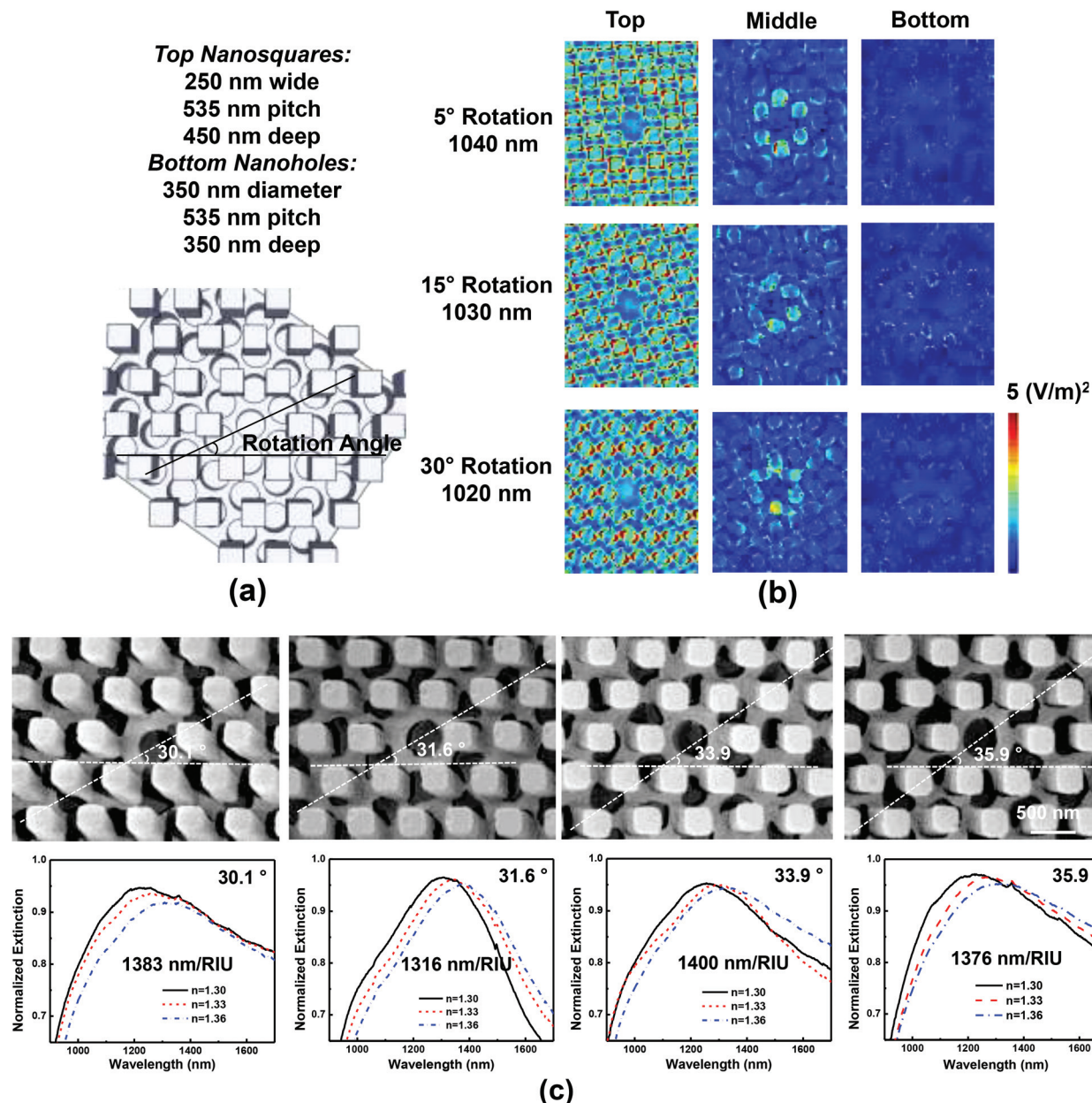


Fig. 5 (a) Schematic of 3D plasmonic photonic crystal nanostructures with point-defect cavities. (b) Simulated EM field intensity distributions of 3D plasmonic photonic crystal nanostructures with point-defect cavities and different rotation angles. (c) Micrographs and measured sensitivity of 3D plasmonic photonic crystal nanostructures with point-defect cavities and different rotation angles.

These results indicate that the variation in rotation angles had negligible effect in the performance of this LSPR biosensor. The micrographs and measured sensitivity of the 3D PPC nanostructures with point-defect cavities and different rotation angles are shown in Fig. 5(c). As the rotation angle changed from 30.1° to 35.9°, there was only minor changes in the resonance wavelength and sensitivity of these 3D PPC nanostructures with point-defect cavities. The average sensitivity of 3D PPC nanostructures with point-defect cavities and different rotation angles was 1376 nm RIU⁻¹, as shown in Fig. 6. As shown in Fig. 6(a), two resonance peaks at 564 and 1232 nm

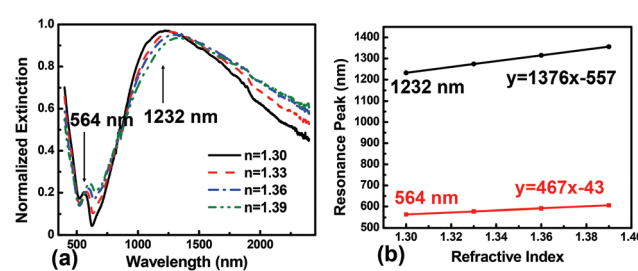


Fig. 6 (a) Extinction spectra and (b) resonance peak as a function of the refractive index in the surrounding area of 3D plasmonic photonic crystal nanostructures with defect cavities.

were observed in liquid with RI of 1.30. All resonance peaks and valleys linearly red-shifted as the RI of the liquids increased from 1.30 to 1.39. The measured sensitivities of the resonance peaks at 564 and 1232 nm were 467 and 1376 nm RIU⁻¹, respectively, as shown in Fig. 6(b). Compared with that of 2D and quasi-3D Au nanoholes, the sensitivity of 3D PPC nanostructures with point-defect cavities had increased to 1376 nm RIU⁻¹. Moreover, the FOM of the resonance peak at 564 nm was as high as 11.6. Hence, the hybrid plasmonic and photonic crystal modes with three-layer plasmonic nanostructures increased the sensitivity of the 3D PPC nanostructures with point-defect cavities to levels higher than that of 2D and quasi-3D plasmonic nanostructures. The FOM and quality factor of 3D PPC nanostructures could be further improved by using gain-assisted cavities⁵⁵ and low loss plasmonic materials^{56–58} to reduce LSPR damping. This result indicates that 3D PPC nanostructures with point-defect cavities could be used as high-performance LSPR biosensors.

3.3 Detection of fibroblast L cell-derived exosomes with 3D PPC biosensor

The performance of the 3D PPC biosensor in the detection of fibroblast L cell-derived exosomes was investigated. The micrographs of fibroblast L cell-derived exosomes on a flat Au surface and on the 3D PPC biosensor are shown in Fig. 7(a and b). The flat Au surface and 3D PPC biosensors were functionalized with anti-EpCAM antibody to enable exosome capture. The exosomes had immune absorption rather than simple Langmuir absorption because the EpCAM on the surface of exosomes would bind to the anchored anti-EpCAM

on the Au film.⁵⁹ The interaction between streptavidin and biotin was the strongest known non-covalent interactions with dissociation constant (K_d) of 10^{-15} M between protein and ligand.⁶⁰ As shown in Fig. 7(a and b), the fibroblast L cell-derived exosome exhibited an elliptical shape on the flat Au surface and a spread out shape on the 3D PPC biosensors by attaching intervesicular filaments around the 3D nanostructures. Given that localized SPs were mainly enhanced around the top nanosquares of 3D PPC nanostructures for the resonance peak at longer wavelength, the exosomes on the 3D nanostructures were in contact with a larger plasmon sensing area compared to exosomes on flat surface, thus increasing the detection sensitivity of exosomes by the 3D PPC biosensor. The exosomes were captured on the surface of the 3D PPC biosensor. More exosomes filled in the point defect cavities at higher concentration and most of the cavities were filled at 1×10^9 particles per ml. ESI Fig. S4† shows the exosome size distribution. The average size of fibroblast L cell-derived exosomes was 230 nm. Furthermore, the size and the spacing between the top SU-8 nanosquares were comparable with these fibroblast L cell-derived exosomes. Hence, the detection range of exosome concentration by our 3D PPC biosensor increased because exosomes had larger contact area on the 3D plasmonic nanostructures. The normalized extinction spectra of the 3D PPC biosensor in the absence of exosomes and in the presence of exosomes at the concentrations of 1×10^5 and 1×10^{11} particles per ml are shown in Fig. 7(c). The functionalization of the 3D PPC biosensor with 20 μ l of anti-EpCAM resulted in the 6 nm peak shift for the resonance peak at 1082 nm. In comparison, exosome detection based on surface plasmon resonance⁶¹ and microfluidic technique⁶² require a larger sample volume of 378 μ l and fluorescence labeling, respectively, and could only detect the relative value of exosome concentration. By contrast, the 3D PPC biosensor could quantitatively detect the concentration of exosomes in the range of 1×10^4 – 1×10^{11} particles per ml with high sensitivity. Since the anchored anti-EpCAM on the Au surface had higher potential than EpCAM on the exosomes, exosomes binding could occur over a wide concentration range from 1×10^4 – 1×10^{11} particles per ml. The resonance peak shift as a function of exosome concentration is shown in Fig. 7(d). A large peak shift of 9 nm was observed during the detection of exosomes at the concentration of 1×10^4 particles per ml, and the peak shift increased to 102 nm when exosome concentration increased to 1×10^{11} particles per ml because of the high sensitivity of this 3D PPC biosensor.

4. Conclusions

We had systematically investigated 2D, quasi-3D, and 3D PPC nanostructures with point-defect cavities. The asymmetrical 2D Au nanoholes showed two resonance peaks at 661 and 814 nm that were attributed to SPPs and LSPR. The measured sensitivity of the resonance peak at 814 nm was 276 nm RIU⁻¹. Compared with those of the 2D Au nanoholes, the EM field

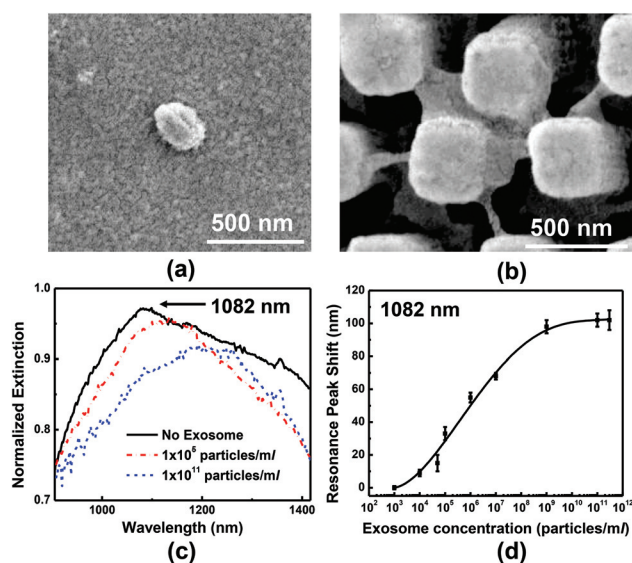


Fig. 7 Micrographs of exosomes on (a) flat Au surface and (b) 3D plasmonic photonic crystal biosensor at concentration of 1×10^6 particles per ml. (c) Extinction spectra of 3D plasmonic photonic crystal biosensor without exosome and with 1×10^5 and 1×10^{11} particles per ml exosomes. (d) Resonance peak shift as a function of exosome concentration.

intensity and sensitivity of the quasi-3D Au nanoholes increased through the hybrid coupling of LSPR and Fabry-Perot cavity modes. At 674 and 1406 nm, the symmetrical quasi-3D Au nanoholes exhibited two resonance peaks and the sensitivity of 100 and 483 nm RIU⁻¹, respectively. In addition, the symmetry breakage of the quasi-3D Au nanoholes could further increase sensitivity to 946 nm RIU⁻¹ by enhancing EM field intensity around corners and by generating an additional quadrupole plasmon mode, which is a dark subradiant mode. The FOM values of the symmetrical and asymmetrical quasi-3D Au nanoholes were 0.8 and 2.4, respectively. The 3D PPC nanostructures with point-defect cavities showed the highest sensitivity of 1376 nm RIU⁻¹ for the resonance peak at 1232 nm and the highest FOM of 11.6 for the resonance peak at 564 nm. These results are attributed to the hybrid plasmonic and photonic crystal modes in the 3D plasmonic nanostructures. The detection sensitivity of the 3D PPC biosensor increased because the 3D nanostructures increase the sensing area of fibroblast L cell-derived exosomes. Thus, a large peak shift of 9 nm was observed during the detection of exosomes at the concentration of 1×10^4 particles per ml, and the peak shift increased to 102 nm when exosome concentration increased to 1×10^{11} particles per ml.

Conflicts of interest

There are no conflicts to declare.

Acknowledgements

We gratefully acknowledge Mr AU-YEUNG Allan Sung King for providing fibroblast L Cells exosomes. This work was supported by the Center for Biosystems, Neuroscience, and Nanotechnology (CBNN) of City University of Hong Kong (9360148, 9380062), the University Grants Council of Hong Kong (GRF Projects: 11210814, 11247716, and 11218017 and CRF project: C1013-15). We also thank all the members of CBNN and university cleanroom facilities for their help.

References

- K. Skriner, K. Adolph, P. R. Jungblut and G. R. Burmester, *Arthritis Rheum.*, 2006, **54**, 3809–3814.
- L. Cheng, R. A. Sharples, B. J. Scicluna and A. F. Hill, *J. Extracell. Vesicles*, 2014, **3**, 23743–23757.
- W. Zhou, M. Y. Fong, Y. Min, G. Somlo, L. Liu, M. R. Palomares, Y. Yu, A. Chow, S. T. O'Connor, A. R. Chin, Y. Yen, Y. Wang, E. G. Marcusson, P. Chu, J. Wu, X. Wu, A. X. Li, Z. Li, H. Gao, X. Ren, M. P. Boldin, P. C. Lin and S. E. Wang, *Cancer Cell*, 2014, **25**, 501–515.
- K. E. Richards, A. E. Zeleniak, M. L. Fishel, J. Wu, L. E. Littlepage and R. Hill, *Oncogene*, 2017, **36**, 1770–1778.
- J. den Toonder, *Lab Chip*, 2011, **11**, 375–377.
- J. Ko, E. Carpenter and D. Issadore, *Analyst*, 2016, **141**, 450–460.
- S. L. Stott, R. J. Lee, S. Nagrath, M. Yu, D. T. Miyamoto, L. Ulkus, E. J. Inserra, M. Ulman, S. Springer and Z. Nakamura, *Sci. Transl. Med.*, 2010, **2**, 25ra23–25ra23.
- E. van der Pol, M. J. van Gemert, A. Sturk, R. Nieuwland and T. G. van Leeuwen, *J. Thromb. Haemostasis*, 2012, **10**, 919–930.
- P. R. Rocha, P. Schlett, U. Kintzel, V. Mailander, L. K. Vandamme, G. Zeck, H. L. Gomes, F. Biscarini and D. M. de Leeuw, *Sci. Rep.*, 2016, **6**, 34843–34853.
- Y. Yuana, T. H. Oosterkamp, S. Bahatyrova, B. Ashcroft, P. Garcia Rodriguez, R. M. Bertina and S. Osanto, *J. Thromb. Haemostasis*, 2010, **8**, 315–323.
- B. Vestad, A. Llorente, A. Neurauter, S. Phuyal, B. Kierulf, P. Kierulf, T. Skotland, K. Sandvig, K. B. F. Haug and R. Ovstebo, *J. Extracell. Vesicles*, 2017, **6**, 1344087–1344098.
- M. E. Stewart, N. H. Mack, V. Malyarchuk, J. A. Soares, T. W. Lee, S. K. Gray, R. G. Nuzzo and J. A. Rogers, *Proc. Natl. Acad. Sci. U. S. A.*, 2006, **103**, 17143–17148.
- P. K. Jain, W. Huang and M. A. El-Sayed, *Nano Lett.*, 2007, **7**, 2080–2088.
- M. I. Stockman, *Science*, 2015, **348**, 287–288.
- C. Lee, R. P. Carney, S. Hazari, Z. J. Smith, A. Knudson, C. S. Robertson, K. S. Lam and S. Wachsmann-Hogiu, *Nanoscale*, 2015, **7**, 9290–9297.
- H. Im, H. Shao, Y. I. Park, V. M. Peterson, C. M. Castro, R. Weissleder and H. Lee, *Nat. Biotechnol.*, 2014, **32**, 490–495.
- F. Liu, M. M. Wong, S. K. Chiu, H. Lin, J. C. Ho and S. W. Pang, *Biosens. Bioelectron.*, 2014, **55**, 141–148.
- X. Zhao, M. M.-K. Wong, S.-K. Chiu and S. W. Pang, *Biosens. Bioelectron.*, 2015, **74**, 799–807.
- V. E. Bochenkov, M. Frederiksen and D. S. Sutherland, *Opt. Express*, 2013, **21**, 14763–14770.
- Y. Sonnenfraud, N. Verellen, H. Sobhani, G. A. Vandenbosch, V. V. Moshchalkov, P. Van Dorpe, P. Nordlander and S. A. Maier, *ACS Nano*, 2010, **4**, 1664–1670.
- S. Zhu, H. Li, M. Yang and S. W. Pang, *Nanotechnology*, 2016, **27**, 295101–295113.
- J. Cao, T. Sun and K. T. V. Grattan, *Sens. Actuators, B*, 2014, **195**, 332–351.
- S. K. Dondapati, T. K. Sau, C. Hrelescu, T. A. Klar, F. D. Stefani and J. Feldmann, *ACS Nano*, 2010, **4**, 6318–6322.
- L. Y. M. Tobing, L. Tjahjana, D. H. Zhang, Q. Zhang and Q. Xiong, *Sci. Rep.*, 2013, **3**, 2437–2443.
- A. E. Cetin and H. Altug, *ACS Nano*, 2012, **6**, 9989–9995.
- A. Christ, O. J. Martin, Y. Ekinci, N. A. Gippius and S. G. Tikhodeev, *Nano Lett.*, 2008, **8**, 2171–2175.
- J. H. Cho and D. H. Gracias, *Nano Lett.*, 2009, **9**, 4049–4052.
- F. Hao, Y. Sonnenfraud, P. V. Dorpe, S. A. Maier, N. J. Halas and P. Nordlander, *Nano Lett.*, 2008, **8**, 3983–3988.
- P. C. Wu, G. Sun, W. T. Chen, K.-Y. Yang, Y.-W. Huang, Y.-H. Chen, H. L. Huang, W.-L. Hsu, H. P. Chiang and D. P. Tsai, *Appl. Phys. Lett.*, 2014, **105**, 33105–33109.

- 30 T.-W. Chang, X. Wang, A. Hsiao, Z. Xu, G. Lin, M. R. Gartia, X. Liu and G. L. Liu, *Adv. Opt. Mater.*, 2015, **3**, 1397–1404.
- 31 B. Ai, L. Wang, H. Mohwald, Y. Yu and G. Zhang, *Nanoscale*, 2015, **7**, 2317–2324.
- 32 H. H. Jeong, A. G. Mark, M. Alarcon-Correa, I. Kim, P. Oswald, T. C. Lee and P. Fischer, *Nat. Commun.*, 2016, **7**, 11331–11338.
- 33 S. Zhu, H. Li, M. Yang and S. W. Pang, *Nanotechnology*, 2018, **29**, 365503–365516.
- 34 W. Hu, B. Yang, C. Peng and S. W. Pang, *J. Vac. Sci. Technol., B: Microelectron. Nanometer Struct.–Process., Meas., Phenom.*, 2006, **24**, 2225–2229.
- 35 Y. P. Kong, H. Y. Low, S. W. Pang and A. F. Yee, *J. Vac. Sci. Technol., B: Microelectron. Nanometer Struct.–Process., Meas., Phenom.*, 2004, **22**, 3251–3256.
- 36 B. Yang and S. W. Pang, *J. Vac. Sci. Technol., B: Microelectron. Nanometer Struct.–Process., Meas., Phenom.*, 2006, **24**, 2984–2987.
- 37 C. Peng and S. W. Pang, *J. Vac. Sci. Technol., B: Microelectron. Nanometer Struct.–Process., Meas., Phenom.*, 2006, **24**, 2968–2972.
- 38 J.-S. Wi, S. Lee, S. H. Lee, D. K. Oh, K.-T. Lee, I. Park, M. K. Kwak and J. G. Ok, *Nanoscale*, 2017, **9**, 1398–1402.
- 39 C. C. R. Company, *CRC handbook of chemistry and physics*, CRC Press, Taylor & Francis Group, 2007.
- 40 H.-C. Lin, H.-C. Huang and S.-L. Tsao, *Opt. Commun.*, 2005, **250**, 69–76.
- 41 J. Li, S. K. Cushing, P. Zheng, F. Meng, D. Chu and N. Wu, *Nat. Commun.*, 2013, **4**, 2651.
- 42 J. Xu, P. Guan, P. Kvasnička, H. Gong, J. Homola and Q. Yu, *J. Phys. Chem. C*, 2011, **115**, 10996–11002.
- 43 A. Hajaboli, M. Kahrizi and V.-V. Truong, *J. Phys. D: Appl. Phys.*, 2012, **45**, 485105–485109.
- 44 J. Butet, P.-F. Brevet and O. J. Martin, *ACS Nano*, 2015, **9**, 10545–10562.
- 45 J. Yang, Q. Sun, H. Yu, K. Ueno, H. Misawa and Q. Gong, *Photonics Res.*, 2017, **5**, 30187–30193.
- 46 Z. Yi, G. Niu, J. Chen, J. Luo, X. Liu, Y. Yi, T. Duan, X. Kang, X. Ye, P. Wu and Y. Tang, *Plasmonics*, 2015, **11**, 37–44.
- 47 M. Rang, A. C. Jones, F. Zhou, Z.-Y. Li, B. J. Wiley, Y. Xia and M. B. Raschke, *Nano Lett.*, 2008, **8**, 3357–3363.
- 48 W. Zhou and T. W. Odom, *Nat. Nanotechnol.*, 2011, **6**, 423–427.
- 49 D. E. Gomez, Z. Q. Teo, M. Altissimo, T. J. Davis, S. Earl and A. Roberts, *Nano Lett.*, 2013, **13**, 3722–3728.
- 50 J. F. Galisteo-López, M. López-García, C. López and A. García-Martín, *Appl. Phys. Lett.*, 2011, **99**, 083302–083305.
- 51 Z. Liu, M. Yu, S. Huang, X. Liu, Y. Wang, M. Liu, P. Pan and G. Liu, *J. Mater. Chem. C*, 2015, **3**, 4222–4226.
- 52 S. G. Romanov, A. V. Korovin, A. Regensburger and U. Peschel, *Adv. Mater.*, 2011, **23**, 2515–2533.
- 53 J. Vuckovic, M. Loncar, H. Mabuchi and A. Scherer, *Phys. Rev. E: Stat., Nonlinear Soft Matter Phys.*, 2002, **65**, 016608–016619.
- 54 H. A. Atwater and A. Polman, *Nat. Mater.*, 2010, **9**, 205–213.
- 55 P.-J. Cheng, Z.-T. Huang, J.-H. Li, B.-T. Chou, Y.-H. Chou, W.-C. Lo, K.-P. Chen, T.-C. Lu and T.-R. Lin, *ACS Photonics*, 2018, **5**, 2638–2644.
- 56 A. Boltasseva and H. A. Atwater, *Science*, 2011, **331**, 290–291.
- 57 M. Kumar, N. Umezawa, S. Ishii and T. Nagao, *ACS Photonics*, 2015, **3**, 43–50.
- 58 C. Gong and M. S. Leite, *ACS Photonics*, 2016, **3**, 507–513.
- 59 W. Wang, J. Luo and S. Wang, *Adv. Healthcare Mater.*, 2018, 1800484–1800510.
- 60 J. DeChancie and K. N. Houk, *J. Am. Chem. Soc.*, 2007, **129**, 5419–5429.
- 61 B. Hosseinkhani, N. van den Akker, J. D'Haen, M. Gagliardi, T. Struys, I. Lambrechts, J. Waltenberger, I. Nelissen, J. Hooyberghs, D. G. M. Molin and L. Michiels, *Nanomedicine*, 2017, **13**, 1663–1671.
- 62 S. Fang, H. Tian, X. Li, D. Jin, X. Li, J. Kong, C. Yang, X. Yang, Y. Lu, Y. Luo, B. Lin, W. Niu and T. Liu, *PLoS One*, 2017, **12**, e0175050–e0175063.